RESEARCH ARTICLE

A Robustness Temperature Inversion Method for Cable Straight Joints Based on Improved Sparrow Search Algorithm Optimized BPNN

QINGHUA ZHAN[1], JIANGJUN RUAN[1], (Member, IEEE), HESHENG ZHU[2], AND YULI WANG[2]
[1]School of Electrical and Automation, Wuhan University, Wuhan 430072, China
[2]College of Electrical Engineering and New Energy, China Three Gorges University, Yichang 443000, China

Corresponding author: Qinghua Zhan (qhzhan@163.com)

ABSTRACT The temperature of cable conductor is of great significance to improve the current carrying capacity, asset utilization and safe operation of cable lines. Aiming at the problems of slow calculation speed, low accuracy and weak anti-interference ability of the current temperature calculation methods, this paper proposes an inversion method based on improved sparrow search algorithm (ISSA) optimized back propagation neural network (BPNN). Tent mapping was used to increase the initial population diversity of sparrow. Modified sparrow optimization formula to improve convergence speed. Chaotic perturbation is applied to the optimal individual to improve the global and local search ability of SSA. The multi-physics simulation model of 110kv straight connector was established, and the temperature distribution data under three different working conditions were obtained. According to the simulation data and CEC2017 standard test experiments, the optimization ability of the improved model is compared with particle swarm optimization (PSO), whale optimization algorithm (WOA), SSA and MSWOA. To verify the generalization performance and migration ability of the proposed method, the thermal cycle test and inversion calculation of the 10kV cable straight-through joint were carried out. The results show that ISSA-BPNN has high accuracy, fast convergence speed, good robustness, and is less affected by cable joint type, load current and cable environment conditions. It has good engineering practicability.

INDEX TERMS Sparrow search algorithm, BP neural network, tent chaos, cable straight joint, temperature inversion.

I. INTRODUCTION

In response to the green development policy, economic and environmental protection has become the goal of modern power system to transmit electric energy. With the acceleration of urbanization, electricity demand surges. This increase has placed a greater burden on existing lines. Therefore, it is necessary to fully tap the hidden capacity of lines to improve the actual transmission capacity of transmission lines [1], [2]. The capacity of the line depends on the maximum long-term allowable operating temperature of the insulating material. Therefore, the cable core temperature monitoring and diagnosis of line safety evaluation and dynamic thermal rating to determine has an important role in guiding [3], [4], [5], [6].

Cable joints are more prone to overheating due to their physical structure and material properties. There are two main ways to obtain the temperature of the conductor core. One is the implantable temperature measurement, that is, the temperature sensor or optical fiber is buried inside the cable joint when the cable joint is made; the other is non-implantable temperature measurement, such as infrared imaging temperature measurement technology [3], [7], [8], [9]. The built-in temperature measurement unit is at high potential and withstands long-term high temperature, and its safety and stability cannot be guaranteed. When transmitting signals to the external receiving unit module, it will also be interfered by strong electromagnetic fields. Infrared temperature measurement is also susceptible to meteorological factors such as ambient temperature, humidity and wind speed, and the farther the test distance, the lower the

---

The associate editor coordinating the review of this manuscript and approving it for publication was Alireza Sadeghian.

measurement accuracy. These methods are difficult to ensure the safe and stable operation of the joint in the whole life cycle.

In recent years, researchers have conducted a lot of research on the non-invasive indirect calculation method of cable joint temperature. Including thermal circuit method, finite element method (FEM) [10], finite volume method (FVM) [11], [12], boundary element method (BEM) [13], [14] and so on. Gao *et al.* [15] inverted the temperature of cable joint through the second-order transient thermal circuit, and combined with parameter identification for fault diagnosis. Fu *et al.* [16] proposed a fast calculation method for temperature rise of transfer matrix based on finite element data. Although the calculation accuracy has been improved, most of the methods are aimed at a relatively single cable model and laying environment. In the face of new objects and environments, differential equations and simulation models need to be reconstructed. The calculation efficiency is not fast enough and the generalization ability is not strong.

With the development and application of data-driven methods, many artificial intelligence algorithms have been applied to cable joint temperature inversion. Ruan *et al.* [17] used support vector machine (SVM) to invert the temperature of medium and low voltage three-core cable, and verified the accuracy of the inversion effect by measuring multiple positions and temperature measurement points in the experiment. He *et al.* [18] used particle swarm optimization algorithm to optimize the penalty parameter C and kernel function parameter δ of SVM, and predicted the junction temperature by historical temperature, current ratio of core and sheath, etc. Wang *et al.* [19] proposed a joint ampacity estimation algorithm. Fu *et al.* [20] proposed a PSO-Elman neural network method for predicting the temperature of cable conductors. However, the application of machine learning also introduces more hyperparameters which are difficult to solve, resulting in the difficulty of solving the algorithm in some application scenarios, especially when the input characteristics are complex and the dimension is high, overfitting is easy to occur.

The heuristic algorithm is a kind of optimization algorithm developed according to the survival characteristics of organisms. In recent years, new swarm intelligence algorithms such as WOA [21], GWO [22] and SSA have been proposed one after another, and their optimization performance is better. Xu *et al.* [23] used the bird swarm algorithm (BSA) to improve the way sparrows approach the optimal solution and shorten the convergence time of SSA. Li *et al.* [24] proposed a hybrid algorithm combining SSA and genetic algorithm (GA), which introduced logistics chaotic mapping, reverse learning, and Gaussian mutation to enrich the population [25]. This method takes into account the characteristics of strong global search ability of GA and strong local search ability of SSA. N. A. Khan *et al.* [26], [27] combined WOA with the local optimization algorithm Nelder-Mead (MN) to

obtain a hybrid algorithm with shorter time, and performed well in fluid computing and other fields. Li *et al.* [21] introduced Gaussian distribution and adaptive weight to construct the algorithm variant of GDS-WOA, and realized the optimization of constraint problems. Hsu *et al.* [28] used GWO and denoising convolutional neural network (QnCNN) to refine the recognition effect of quaternion discrete cosine transform (QDCT) on image watermark. Zhang *et al.* [29] combined mayfly algorithm (MA) and SSA, introduced levy flight and nonlinear weight to balance the relationship between global search and local search. Tuerxun *et al.* [30] mixed SSA and SVM to improve the accuracy of wind turbines fault diagnosis. There are more other improved models [31], [34], [35], [36]. Although earlier research has increased the algorithm's accuracy and speed of convergence, the global search and local development capabilities of SSA, a recently developed swarm intelligence algorithm, remain uneven and the system is still prone to falling into the local optimum. Additionally, we need to make improvements to it in order to strengthen its robustness and optimize its optimization effect. To deal with complicated and variable operating conditions, the upgraded hybrid algorithm and variant of the swarm intelligence algorithm must be used to the joint temperature inversion.
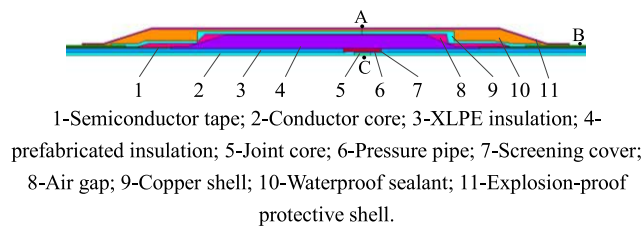
In conclusion, we propose a hybrid approach to enhance SSA and use the improved SSA to optimize the weights and thresholds of BPNN. The common test function CEC2017 assesses the upgraded algorithm's optimization performance. Using modeling and experimental data, the algorithm's impact on the inversion of the cable joint temperature is examined. We assess the performance of the algorithm using δ_{MAE}, δ_{MAPE}, δ_{RMSE}, R_2 four indicators. The outcomes demonstrate that the revised algorithm performs significantly better than the original algorithm.

The main contributions of this study are summarized as follows.

1. A non-destructive testing method for cable joint core temperature based on ISSA-BPNN is proposed. It has a greater inversion accuracy as compared to the PSO, WOA, SSA, and MSWOA optimization models.

2. It is demonstrated that the improved model outperforms the other four models, including the original swarm intelligence algorithm and its variations, in terms of optimization performance by testing and comparing the benchmark functions of high dimension, low dimension, single extremum, and multi-extremum.

3. The performance of each model in cable joint core temperature inversion under different load types in dynamic environment is compared and analyzed. The results show that with the increase of load change rate, the inversion error of each algorithm increases, but the stability of ISSA-BPNN is better.

4. On the test objects of different voltage levels and models, ISSA-BPNN can maintain excellent performance and strong robustness.

TABLE 1. Material parameters of cable straight joint.

Structure Parameter	Material	Density (kg·m^{-3})	Specific Heat Capacity (J·(kg·K)$^{-1}$)	Thermal Conductivity (W·m^{-1}·K^{-1})
conductor	copper	8889	383	401
XLPE	Cross linked polyethylene	920	2500	0.4
semiconductor tape	Polyester fiber	600	2000	0.6
aluminum sheath	aluminum	2780	883	218
outer sheath	Medium density polyethylene	950	1842	0.5
prefabricated insulation	Ethylene Propylene Rubber	1100	2219	0.45
air	air	1.293	1004	0.023
waterproof sealant	Epoxy resin	1050	1750	0.3
explosion-proof protective shell	Glass fiber reinforced plastic	1850	535	1.85

1-Semiconductor tape; 2-Conductor core; 3-XLPE insulation; 4-prefabricated insulation; 5-Joint core; 6-Pressure pipe; 7-Screening cover; 8-Air gap; 9-Copper shell; 10-Waterproof sealant; 11-Explosion-proof protective shell.

FIGURE 1. Structure of single-core 110kV cable straight joint.

II. FINITE ELEMENT SIMULATION OF CABLE JOINTS

A. FINITE ELEMENT SIMULATION MODEL STRUCTURE

The simulation model was constructed with a joint for single-core 110 kV cable with cross-section 630 mm^2 as the object, and its specific structure is shown in Fig.1. Since the structure of the cable joint was axially symmetrical, and the sealing tape, epoxy mud sealing port, grounding structure and other non-completely symmetrical structures had little effect on the distribution of the thermal field of the joint, a two-dimensional axisymmetric model of the joint can be established. In order to improve the simulation efficiency, appropriate equivalent simplification was carried out on the structure of cable joint. Firstly, since the good conductor had little influence on the electrothermal analysis, the anisotropically compressed stranded structure of the cable core conductor was equivalent to a solid cylindrical structure. Secondly, since the semi-conductive shielding layer was thin and similar to the physical parameters of XLPE insulating layer, it was simplified and assumed as a whole together. Finally, the corrugated aluminum sheath was replaced by a ring of equivalent diameter according to the IEC 60287.

B. MATHEMATICAL MODEL OF THERMAL FIELD AND BOUNDARY CONDITIONS

According to the law of conservation of energy, the increase of the internal energy of the cable joint at any time is equal to the difference between the heat generated by the cable itself and the heat dissipated out of the cable joint. In the Cartesian coordinate system, the general form of its constant property, steady state, and two-dimensional thermal differential equation was as follows:

$$\frac{\partial^2 t}{\partial x^2} + \frac{\partial^2 t}{\partial y^2} + \frac{q_v}{\lambda} = 0 \quad (1)$$

where t represents the temperature; q_v is the heat generated by the heat source in the unit time and area; λ is the thermal conductivity.

The solution of the heat conduction equation in (1) also required the initial conditions and boundary conditions as the solution conditions for the partial equations. In the finite element method for partial equation solution, there are three main boundary conditions for the thermal field.

The first boundary conditions: the temperature of the boundary was specified as a constant.

$$t(x, y)|_{\Gamma_1} = f(x, y)|_{\Gamma_1} \quad (2)$$

The second boundary conditions: the heat flux density on the boundary was specified as a fixed value.

$$\lambda \frac{\partial t}{\partial n}\bigg|_{\Gamma_2} = q_n \quad (3)$$

The third boundary condition: the surface heat transfer coefficient h between the object boundary and the surrounding fluid, of which temperature was specified as

$$\lambda \frac{\partial t}{\partial n}\bigg|_{\Gamma_3} = h(t - t_f)|_{\Gamma_3} \quad (4)$$

where Γ_1, Γ_2, Γ_3 is the boundary, n is the normal unit vector of the boundary, h is the convective heat dissipation coefficient, q_n is the heat flux density, t_f is the fluid temperature, and $f(x, y)$ is a constant.

C. PARAMETER AND BOUNDARY CONDITONS SETTING

The material parameters of cable joint is shown in Table. 1. The actual operating environment of the cable joint was complex, and the boundary conditions were difficult to be acquired and determined. When the air velocity around the cable is less than 0.15 m/s, it is a kind of natural convection. The surface of the joint adopted the third type of boundary conditions, the natural convection heat transfer coefficient was set to 8 W/(m^2·°C), and the ambient temperature was set to 20 °C. When the cable conductor at both ends of the joint is more then 5 m, the axial heat conduction is assumed to be in equilibrium state. The simulation results indicated that the axial heat transfer distance of the joint was 2-3 m away from the crimping position of the joint. The total length of the model was 8 m, so both ends can be set to the second
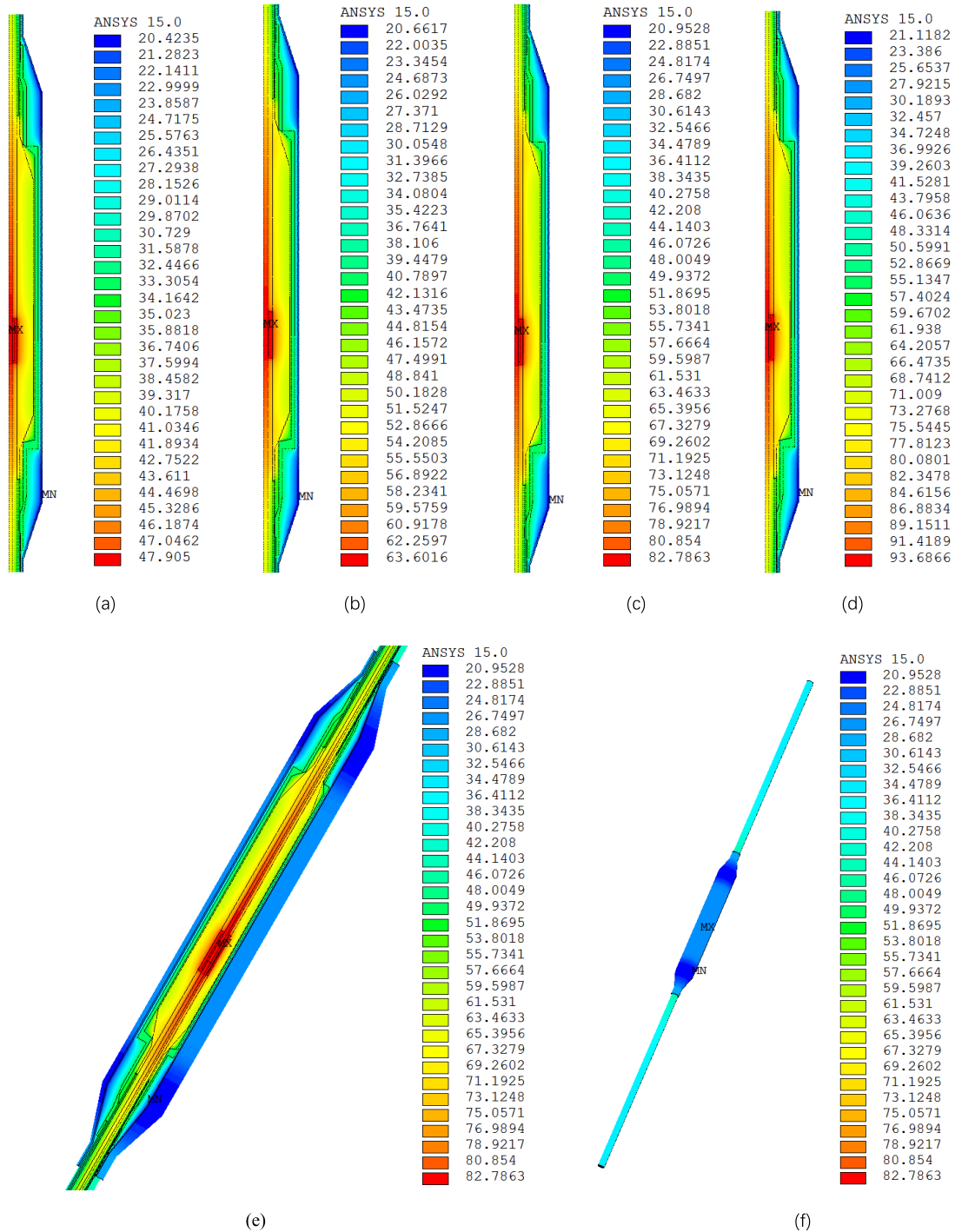
FIGURE 2. Temperature field distribution of cable joints under different load currents. (a) 800A; (b) 1000A; (c) 1200A; (d)1300A; (e)Two-thirds section partial view under1200A; (f) The entire cable joint under 1200A.

boundary conditions, and the normal heat flux density was set to 0 W/m². The excitation of the model is simulated by applying current to generate Joule heat, which was set as reference ground potential at one end of the cable core, and different load currents are loaded at the other end to simulate different working conditions of the actual operation of the cable.

The heat source of a cable joint mainly included the Joule heat of the conductor core, the loss of the insulating medium and the circulation loss of the aluminum sheath. Since the outer sheath of high-voltage cable was cross-connected or single-ended grounded, the circuit current losses were negligible. The Joule heat of the conductor core included the Joule heat of the core itself and the heat generated by the contact
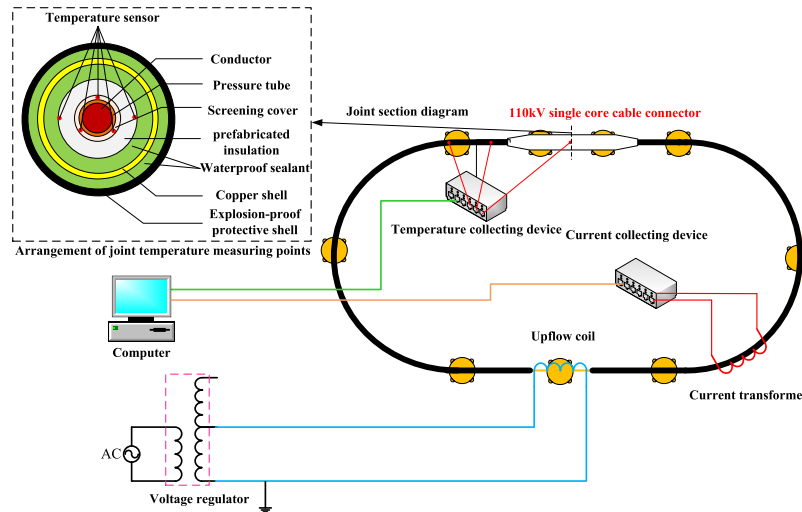
FIGURE 3. The schematic diagram of 110kV cable joint temperature rise test platform.

resistance of the crimping position.

$$P_1 = I^2 R + I^2 R_j \tag{5}$$

$$R = R_{20} \left(1 + \alpha \left(T - 20 \right) \right) \left(1 + Y_s + Y_p \right) \tag{6}$$

where R_{20} is the resistance value of the wire core at 20 °C, α is the temperature coefficient of copper, T is the temperature of the conductor, Y_s and Y_p are the skin effect and the proximity effect factor, respectively, R_j is the contact resistance value of 7×10^{-6}.

The loss of the dielectric loss was calculated according to (7)

$$P_2 = 2\pi f C U^2 \tan\delta \tag{7}$$

where f is the power frequency of voltage, C is the capacitance of insulating layer of cable joint, U is the power frequency voltage and δ is the dielectric loss angle.

D. MODEL SOLVING AND EXPERIMENTAL VERIFICATION

Steady-state temperature distribution of the cable joint under different loads was as shown in Fig.2. It obvious showed that the temperature of the joint crimping position was significantly higher than that of the cable core, and there were different degrees of attenuation along the axial and radial directions. When the connector reaches the allowable long-term thermal operating temperature 90 °C for XLPE, it was inferred that the current carrying capacity of the cable joint was far from being fully utilized.

In this paper, the temperature rise test is carried out by simulating the same type of cable joint. The concept diagram is shown in Fig.3. It is found that the simulation and test data have high consistency for the temperature change of cable conductor. However, as the temperature measurement position is far away from the conductor core, there is a certain difference between the simulation and the experimental data. The temperature rise of the experimental data is faster than

the simulation temperature rise, but the final temperature error between them does not exceed 2 °C, which meets the engineering error requirements.

III. ALGORITHM THEORY

A. SPARROW SEARCH ALGORITHM

In 2020, Xue *et al.* [32] proposed a novel swarm intelligence optimization algorithm-sparrow search algorithm based on natural predatory behaviors of sparrows in biology. The algorithm simulated the process of individual sparrows avoiding predators and constantly approaching the food location. The population was consisted of three roles: producer, follower and early warning. Producers had a high energy reserve and a larger foraging area, which provided foraging area and direction information for the population. Followers approached producers and grabbed food resources. The early warning gave warning signal when danger was appearing, and if necessary, gives up food to avoid danger. The producer location was updated in the following way:

$$X_{i,j}^{t+1} = \begin{cases} X_{i,j}^t \cdot \exp(\frac{-i}{\alpha \times \text{iter}_{\max}}), & R_2 < ST \\ X_{i,j}^t + Q \cdot L, & R_2 \geq ST \end{cases} \tag{8}$$

where, t represents current iterations, $Xt\ i,j$ denotes position information of the j_{th} dimension of the i_{th} sparrow in t iterations, α is a random number in the range of [0, 1], $\text{iter}_{\max}$ is the maximum number of iterations; R_2 takes the value in [0, 1], which represents the warning value; ST takes the value in [0.5, 1], which represents the safety threshold; Q is a random number obeying the standard normal distribution; L is a $1 \times d$ matrix with all elements being 1. When $R_2 < ST$, the population is not in danger and the foraging range of sparrows will increase; when $R_2 \geq ST$, natural enemies appear and the sparrows move to safe areas.

The position update mode of the follower was

$$X_{i,j}^{t+1} = \begin{cases} Q \cdot \exp(\frac{X_w^t - X_{i,j}^t}{i^2}), & i > N/2 \\ X_p^{t+1} + \frac{1}{D} \sum_{j=1}^{D} \left(r \cdot \left(\left| X_{i,j}^t - X_p^{t+1} \right| \right) \right), & i \leq N/2 \end{cases} \tag{9}$$

where N is the population size; X_p is the optimal position occupied by the producer; X_w is the global worst position. $A^+ = A^T(AA^T)^{-1}$, where A is a $1 \times d$ matrix with all elements 1 or -1.

There were a certain number of individuals in producers and followers who need to act as early warning.

$$X_{i,j}^{t+1} = \begin{cases} X_b^t + \beta \cdot \left| X_{i,j}^t - X_b^t \right|, & f_i > f_g \\ X_{i,j}^t + K \cdot \dfrac{\left| X_{i,j}^t - X_w^t \right|}{(f_i - f_w) + \varepsilon}, & f_i = f_g \end{cases} \tag{10}$$

where X_b is the global optimal position; β is the step size, which i is a standard normal distribution random number; K is a random number of $[-1, 1]$; f_i is the current sparrow's fitness value; f_w and f_g are the worst and optimal current global fitness values respectively; ε is the minimum constant to avoid zero denominator; when $f_i = f_g$, individuals in the middle position found danger and update their position; when $f_i > f_g$, individuals at the edge warn and update their position.

B. IMPROVED SPARROW SEARCH ALGORITHM

1) POSITION UPDATE FORMULAS

Two update methods in solving optimization problems were usually applied by approaching to the origin point and a optimal solution, and gained excellent performance where the optimal value was near the origin point. Since the followers approached the optimal solution by jumping to the vicinity of the optimal position, it may cause too much difference between certain dimensions, which limited the algorithm's ability to find the optimal solution. Accordingly, position update formulas for followers and early warnings were modified to (11) and (12), so that individuals moved to the optimal position in the whole solution space.

$$X_{i,j}^{t+1} = \begin{cases} Q \cdot \exp(\frac{X_w^t - X_{i,j}^t}{i^2}), & i > N/2 \\ X_p^{t+1} + \frac{1}{D} \sum_{j=1}^{D} \left(r \cdot \left(\left| X_{i,j}^t - X_p^{t+1} \right| \right) \right), & i \leq N/2 \end{cases} \tag{11}$$

$$X_{i,j}^{t+1} = \begin{cases} X_b^t + \beta \cdot \left| X_{i,j}^t - X_b^t \right|, & f_i > f_g \\ X_{i,j}^t + K \cdot \left| X_{i,j}^t - X_w^t \right|, & f_i = f_g \end{cases} \tag{12}$$

where D is the population dimension and r is a random number of $[-1,1]$

2) TENT CHAOTIC MAPPING

Generally, swarm intelligence algorithms were randomly initialized populations, but the uniformity of population was stochastic distribution in space. The initial population distribution affected the convergence speed and accuracy of the algorithm. [33], [34]. At the later period of iteration, SSA still had the common problem of swarm intelligence algorithm. The population approached to the food location, the foraging space shrinks, the population diversity decreased, and the algorithm was easy to fall into the local optimal solution. The randomness of chaotic mapping could enrich population diversity and improve the ability of the algorithm to jump out of local optimum. The common chaos operators included logistic mapping and tent mapping, etc. However, the probability of logistic mapping in the interval of [0,0.1] and [0.9,1] was much higher than the probability of the middle position. By comparison, the mapping generated by tent chaos mapping in the interval of [0,1] had better ergodic and uniformity. In terms of processing large-scale data, the iteration speed was also more faster [35], [36]. In addition, to overcome the shortcomings of traditional tent chaotic mapping and avoid chaotic particles falling into small period and unstable period points during iteration [35], a random variable was added to the original mapping formula, and the modified Tent chaotic mapping was expressed as follows.

$$x_{i+1} = \begin{cases} 2x_i + \text{rand}(0, 1)/N & 0 \leq x_i < 0.5 \\ 2(1 - x_i) + \text{rand}(0, 1)/N & 0.5 < x_i \leq 1 \end{cases} \tag{13}$$

The chaotic values obtain from equation (13) were mapped to the sparrow population as follow

$$x_{d,n} = lb + x_d (ub - lb) \tag{14}$$

where $x_{d,n}$ is a new value of the chaotic sequence carrier to the population space; u_b and l_b are upper and lower bounds of the sparrow position, respectively; x_d is a chaotic variable.

Then equation (13) was used to perturb the local optimal individuals of the population and retained the optimal position

$$x_n = (x + x_{d,n})/2 \tag{15}$$

where, x_n is the individual after perturbation; x is the individual to be perturbed.

C. BACK PROPAGATION NEURAL NETWORK

The basic topological structure of BPNN, shown in Fig.4, consists of an input layer, a hidden layer, and an output layer.

BPNN is a multi-layer feed-forward network trained according to the error back propagation algorithm, which has the advantages of strong nonlinear mapping capability and flexible network structure. The forward propagation of the information of the input feature quantity is processed by the hidden layer to obtain the actual output. If the error between the output value and the expected value does not meet the set operation termination condition, the error is propagated from the output layer forward layer by layer, and the gradient descent method is adopted. Through the adjustment of the weights and thresholds of the hidden layer neurons and the connected neurons, the network training is
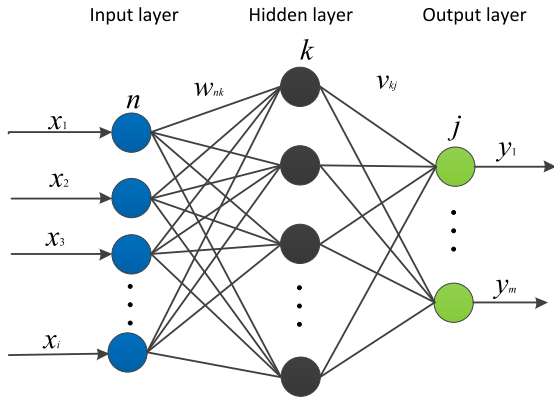
Input layer   Hidden layer   Output layer

FIGURE 4. Topological structure of BPNN.

stopped until the error setting condition or the maximum number of iterations is reached. The specific training steps for the network are as follows:

(1) Initialize the hyperparameters of the network, including the network weights w_{nk}, v_{kj} and thresholds a, b.

(2) Calculate the output value of hidden layer neurons q_k.

$$q_k = f\left(\sum_{n=1}^{i} w_{nk} x_n - a_k\right) \qquad (16)$$

where $k = 1, 2, \ldots, h$. f is the activation function of the hidden layer. x_n is the nth input.

(3) Calculate the output value of the output layer neurons o_j.

$$o_j = f\left(\sum_{k=1}^{h} v_{kj} q_k - b_j\right) \qquad (17)$$

where $j = 1, 2, \ldots, m$.

(4) Update the weights and thresholds of the network.

$$w_{nk}(t+1) = w_{nk}(t) + \eta q_k (1-q_k) x_n \sum_{j=1}^{m} v_{kj}(y_j - o_j) \qquad (18)$$

$$v_{kj}(t+1) = v_{kj}(t) + \eta q_k (y_j - o_j) \qquad (19)$$

$$a_k(t+1) = a_k(t) + \eta q_k (1-q_k) \sum_{j=1}^{m} v_{kj}(y_j - o_j) \qquad (20)$$

$$b_j(t+1) = b_j(t) + (y_j - o_j) \qquad (21)$$

where η is learning rate, which is between 0 and 1.

(5) Determine whether the iteration termination condition is reached. If not, return to the second step.

IV. CABLE JOINT TEMPERATURE INVERSION MODEL

Considering that service life of the high-voltage cable joints was different, surrounding and aging degree, the acquisition of internal structural material parameters may cause irreversible damage to the joint structure, and the sample size of each operating condition was insufficient [37], [38]. So, this paper takes the operation monitoring data of a power supply

company in China as reference, the finite element simulation of 110 kV cable joint was constructed and the thermal cycle test of 10 kV cable joint was carried out to obtain sufficient training samples.

A. DATA COLLECTION FOR TEMPERATURE INVERSION

The cable joint core temperature depended on the dynamic balance relationship between heat generation and heat dissipation in a cable joint. Therefore, the load currents and the external surface temperatures of the cable joint end (T_B), which were easy to measure and can reflect the relationship between the heat generation and heat dissipation, were selected as input characteristics, and the temperature of the joint core (T_C) was the inversion results. To verify the performance of the temperature inversion method based on ISSA-BPNN, The simulation and test were carried out to obtain the joint temperature data of the following four operating conditions for inversion.

(1) Simulation load currents were applied in the form of a single step to simulate the actual cable line load stabilization period. Temperature rises of the joints were not large when the load current was small, and there was no over-temperature danger. Therefore, load currents were set from 800 A to 1300 A, with 100 A interval for a total of five groups of simulations.

(2) The current was applied in the form of multiple steps with no fixed time interval and large changes. In simulation such as winter and summer periods with large fluctuations in daily electricity consumption, The relation between joint temperatures and currents applied were as shown in Fig.5.

(3) To better simulating the actual operating currents, the actual daily load curve of a residential area was simulated by a segmentation function with one hour interval, and Wave-forms of straight joint temperatures of joints and equivalent current were as shown in Fig.6.

(4) To verify the generalization capability of the algorithm, a single-core cold-shrink straight joint of 10 kV 185 mm^2 was subjected to a thermal cycling test and surface temperature inversion to verify the current and the measured temperature of each layer of the joint were as shown in Fig.7.

Under each of the above operating conditions, the ambient temperature range was set to 18~23 °C. 80% of the simulation test data were randomly selected as the training set and 20% as the test set, and the specific number of samples collected was shown in Table 2.

B. IMPROVED TEMPERATURE INVERSION MODEL CONSTRUCTION

Due to the high sensitivity of BPNN to weight and threshold values [39]. In the continuous iteration, if the return error is large, the autonomous learning time consuming will be greatly increased. Therefore, in this paper, ISSA was used to optimize the weights and thresholds of BPNN to reduce the
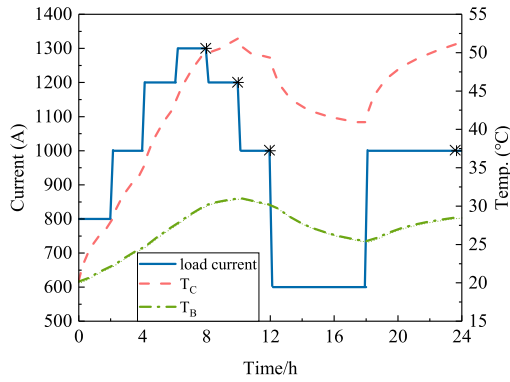
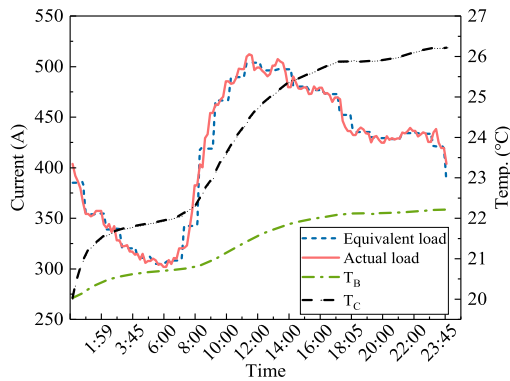**FIGURE 5.** Cable joint temperature under Multi-step load currents.

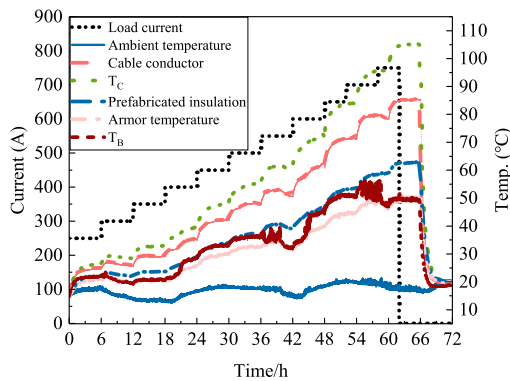**FIGURE 6.** Joint temperature under equivalent load currents.

FIGURE 7. The relation between load currents and temperature at different layers of 10kV cable joint.

TABLE 2. Data sets.

Variants	Sample total	Training set	Testing set
Condition 1	600	500	100
Condition 2	120	100	20
Condition 3	120	100	20
Condition 4	2640	2200	440

training time of networks. The flow chart of the temperature inversion of cable straight joint based on ISSA-BPNN was as showed in Fig.8, and specific processes were as follows:

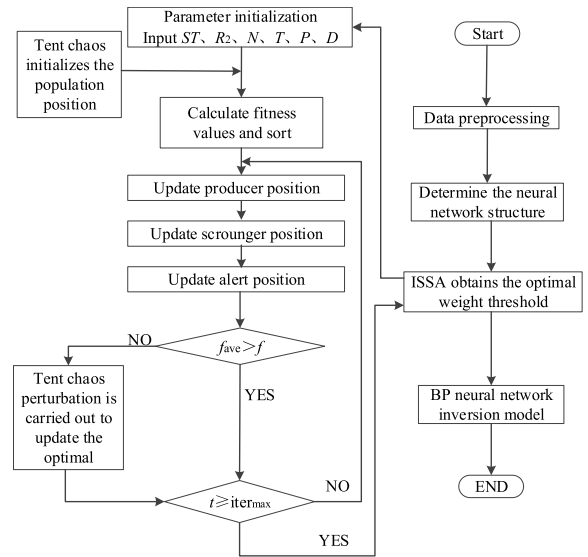(1) Sample data preprocessing to determine the neural network topology.

FIGURE 8. The flow chart temperature inversion based on ISSA-BPNN for cable joints.

(2) Initialization of sparrow population parameters: input population size, the maximum number of iterations, number of discoverers, number of early warning, safety threshold, alarm value.

(3) Tent chaos initialization of population locations.

(4) Calculation and ranking of fitness values for each sparrow.

(5) Update the positions of producers, followers and early warnings.

(6) Determine whether the fitness value reaches the convergence condition, and perform a chaotic perturbation update if it was not reached.

(7) If the maximum number of iterations was reached, the position information of the global optimal sparrow was output, and vice versa, returned to the fifth step to continue the cycle.

(8) Assigning the optimal parameters obtained by SSA to the weights and thresholds of the neural network for temperature inversion.

C. ALGORITHM PERFORMANCE EVALUATION INDEX
Based on the results of temperature inversion, the five models were compared using δ_{MAE} (mean absolute error), δ_{MAPE} (mean absolute percentage error), δ_{RMSE} (root mean square error), and R_2 (goodness of fit) as model evaluation indexes with the following equations:

$$\delta_{\mathrm{MAE}} = \frac{1}{n}\sum_{i=1}^{n}\left|y_p - y_i\right| \tag{22}$$

$$\delta_{\mathrm{MAPE}} = \frac{1}{n}\sum_{i=1}^{n}\left|\frac{y_p - y_i}{y_i}\right| \tag{23}$$

$$\delta_{\mathrm{MSE}} = \frac{1}{n}\sum_{i=1}^{n}\left(y_p - y_i\right)^2 \tag{24}$$

TABLE 3. Benchmark function.

Number	Function formula	Dimension	Range	Optimal value
F1	$f_1 = \sum_{i=1}^{n} x_i^2$	30	[-100,100]	0
F2	$f_2 = \sum_{i=1}^{n} |x_i| + \prod_{i=1}^{n} |x_i|$	30	[-10,10]	0
F3	$f_3 = \sum_{i=1}^{n} \left(\sum_{j=1}^{i} x_j \right)^2$	30	[-100,100]	0
F4	$f_4 = \sum_{i=1}^{n-1} \left[100 \left(x_{i+1} - x_i^2 \right)^2 + \left(x_i - 1 \right)^2 \right]$	30	[-30,30]	0
F5	$f_5 = \sum_{i=1}^{n} -x_i \sin\left(\sqrt{|x_i|} \right)$	30	[-500,500]	418.9829D
F6	$f_6 = -20\exp\left(-0.2\sqrt{\frac{1}{n}\sum_{i=1}^{n} x_i^2} \right) - \exp\left(\frac{1}{n}\sum_{i=1}^{n} \cos\left(2\pi x_i \right) \right) + 20 + e$	30	[-32,32]	0
F7	$f_7 = -\sum_{i=1}^{5} \left[\left(X - a_i \right)\left(X - a_i \right)^T + c_i \right]^{-1}$	4	[0,10]	-10.5363
F8	$f_8 = 4x_1^2 - 2.1x_1^4 + \frac{1}{3}x_1^6 + x_1 x_2 - 4x_2^2 + 4x_2^4$	2	[-5,5]	-1.0316
F9	$f_9 = \sum_{i=1}^{11} \left[a_i - \frac{x_1 \left(b_i^2 + b_i x_2 \right)}{b_i^2 + b_i x_3 + x_4} \right]^2$	4	[-5,5]	0.000307

$$R^2 = 1 - \frac{\sum_{i=1}^{n} \left(y_p - y_i \right)^2}{\sum_{i=1}^{n} \left(y_i - y_{i,ave} \right)^2} \qquad (25)$$

where n is the number of inversion samples, y_p is the model inversion value, y_i is the actual value, and $y_{i.ave}$ is the average of the actual values.

V. RESULTS AND DISCUSSION

A. ALGORITHM OPTIMIZATION EXPERIMENT BASED ON CEC2017

To verify the optimization ability of the improved algorithm in this paper, the ISSA is compared with the SSA, PSO, WOA and MSWOA (Introducing sobol chaos and adaptive weight) [40] algorithms on the nine benchmark functions of CEC2017. The specific test functions are shown in Table 3. F1-F4 are high-dimensional unimodal functions, F5 and F6 are high-dimensional multimodal functions, F7-F9 are low-dimensional multimodal functions. For avoiding accidental errors, we run 30 times on each benchmark function independently, and select the best value, average value and standard deviation as evaluation indexes. In the experiment, the population size is set to 30, and the maximum number of iterations is 250. The results are shown in Table 4. To compare the convergence speed and accuracy of each algorithm model more

intuitively, this paper also gives the test function convergence curve shown in Fig.9.

On F1-F4, the optimization effect of ISSA is better than that of PSO, WOA, SSA and MSWOA. For F1, SSA, MSWOA and ISSA can find their optimal values, but the average and standard deviation of ISSA are 0, indicating that it has strong stability. The optimization effect of ISSA on F2 is also tens of orders of magnitude higher than other algorithms. According to the overall performance of the model on the single-extremum test function, it can be seen that it has certain advantages over other swarm intelligence optimization algorithms in its local development ability. On the F5 function, although the algorithm failed to find the ideal optimal solution, but the convergence curve shows that the convergence rate of ISSA is still faster. This is because chaos perturbation enriches the population individuals and improves the global search efficiency. The variants of the swarm intelligence algorithm on F6-F9 can find the optimal value, indicating that the ISSA and MSWOA algorithms have better optimization capabilities under low-dimensional conditions. The convergence speed of ISSA in Fig.9 (a) (b) (c) (e) (f) is faster. In addition, the convergence speed of ISSA and MSWOA in the convergence graph is not much different, but the convergence speed of the improved swarm intelligence algorithm model is significantly faster than that of the original swarm intelligence algorithm.

TABLE 4. Comparison of benchmark function test results.

Number	Algorithm	Optimum value	Average value·	standard deviation
F_1	PSO	5.204E-04	3.764E-02	8.437E-02
	WOA	4.516E-29	6.128E-27	8.237E-27
	SSA	0	2.452E-32	6.423E-32
	MSWOA	0	7.237E-95	4.765E-94
	ISSA	0	0	0
F_2	PSO	3.465E-07	9.156E-05	8.935E-05
	WOA	1.265E-23	6.984E-19	4.686E-20
	SSA	6.152E-31	7.164E-23	2.987E-22
	MSWOA	1.687E-78	6.893E-69	3.985E-68
	ISSA	4.698E-234	7.165E-231	9.465E-230
F_3	PSO	3.469E05	6.158E06	1.864E07
	WOA	9.165E-02	5.189E02	6.795E03
	SSA	6.564E-04	3.372E-02	6.782E-02
	MSWOA	4.285E-06	6.542E-04	3.489E-03
	ISSA	3.968E-16	4.897E-13	7.156E-13
F_4	PSO	1.564E04	3.183E07	9.896E07
	WOA	5.166E01	2.468E02	3.457E02
	SSA	6.546E01	4.238E02	3.487E02
	MSWOA	1.157E01	1.273E01	1.186E01
	ISSA	0.756E01	2.452E01	1.895E01
F_5	PSO	-7.346E03	-5.134E03	1.538E03
	WOA	-1.216E04	-1.134E04	1.657E03
	SSA	-9.064E03	-7.648E03	7.264E02
	MSWOA	-8.063E03	-7.649E03	6.913E02
	ISSA	-8.643E03	-6.453E03	6.843E02
F_6	PSO	1.946E-02	1.339E00	7.158E-01
	WOA	4.841E-15	3.194E-14	1.824E-14
	SSA	8.234E-16	7.166E-16	4.727E-17
	MSWOA	8.882E-16	8.882E-16	0
	ISSA	8.882E-16	8.882E-16	0
F_7	PSO	-1.054E01	-5.537E00	3.548E00
	WOA	-1.054E01	-7.164E00	3.164E00
	SSA	-1.054E01	-7.658E00	2.354E00
	MSWOA	-1.054E01	-1.054E01	0
	ISSA	-1.054E01	-1.054E01	0
F_8	PSO	-1.032E00	-1.032E00	3.789E-04
	WOA	-1.032E00	-1.032E00	7.858E-08
	SSA	-1.032E00	-1.032E00	3.457E-10
	MSWOA	-1.032E00	-1.032E00	4.537E-15
	ISSA	-1.032E00	-1.032E00	2.453E-17
F_9	PSO	3.705E-04	1.254E-03	3.452E-03
	WOA	3.154E-04	1.374E-03	3.745E-03
	SSA	3.075E-04	3.157E-03	1.104E-04
	MSWOA	3.241E-04	3.894E-04	4.531E-05
	ISSA	3.075E-04	3.075E-04	9.453E-11

F8 function for each algorithm is easy to find its optimal solution in the beginning of the iteration directly converges to the optimal solution, so the graph is almost a straight line. In summary, it can be proved that the optimization performance of ISSA has been significantly improved, and the stability is also strong.

B. TEMPERATURE INVERSION PERFORMANCE UNDER DIFFERENT LOAD CURRENTS

To intuitively evaluate the optimization performance of ISSA in the proposed cable joint temperature inversion method based on ISSA-BPNN, it is compared with PSO, WOA, SSA and MSWOA optimization algorithms. To ensure the fairness of temperature inversion experiments, the population for the first iteration used is the same for all algorithms. the

population of all algorithms is set to 50, the maximum number of iterations is 100, and the remaining parameters are set as shown in Table 5. BPNN uses relu as the hidden layer activation function. The input layer and output layer nodes are 2 and 1 respectively, and the number of hidden layers is 1. The number of neurons is determined to be 9 according to the empirical formula (26) and the mean square error on the training set. The average mean square error on the training set and the test set is selected as the fitness function, as shown in Equation (27).

$$h = \sqrt{m+n} + a \quad (26)$$

$$f = \frac{1}{2}\left[\frac{1}{M}\sum_1^M \left(y_p - o_p\right)^2 + \frac{1}{N}\sum_1^N \left(Y_T - O_T\right)^2 \right] \quad (27)$$
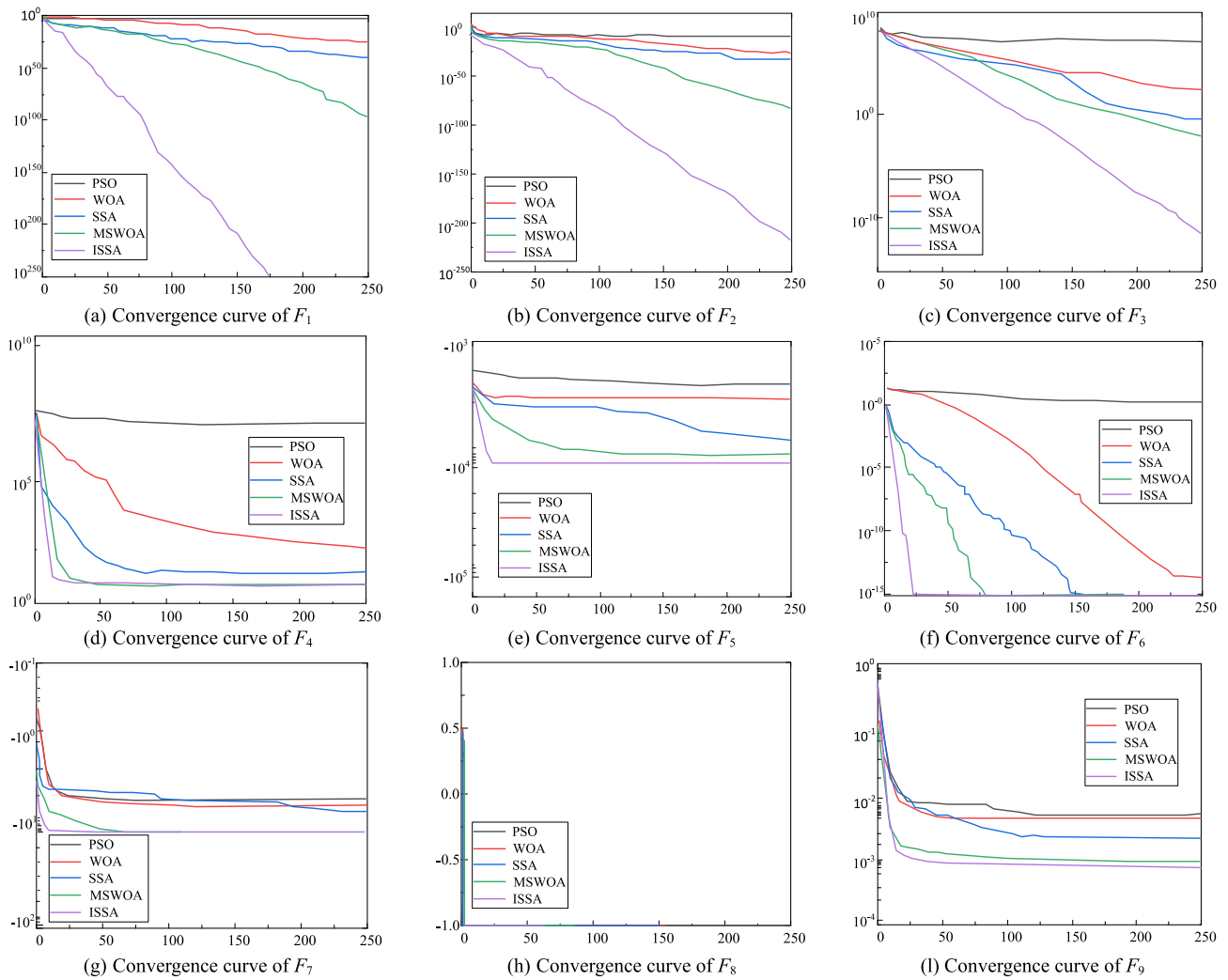
FIGURE 9. Test function convergence curve of F1-F9.

TABLE 5. Algorithm parameter settings.

Algorithm	Parameters
PSO	$c_1=c_2=1.5$, $w=1$
WOA	$b=1$
SSA	$ST=0.8$, $P=0.8$, $D=0.2$
MSWOA	$a \in [0,2]$, $b=1$
ISSA	$ST=0.8$, $P=0.8$, $D=0.2$

where n is the number of neurons in the input layer, m is the number of neurons in the output layer, and a is the constant between [1,10]. M and N are the sample numbers of training set and test set respectively; y_p, o_p is the actual output and expected output under the training sample; Y_T, O_T is the actual output and expected output for the test sample.

Taking the single step optimization results as an example, the fitness curves of five optimization algorithms are compared, as shown in Fig.10. PSO and WOA are stable at 0.103 and 9.1×10^{-2} after 27 and 26 iterations, respectively. SSA converges to 8.3×10^{-2} after 34 iterations. ISSA

and MSWOA converge after 21 iterations, but the former converges to 6.7×10^{-2}, and the convergence accuracy is higher. The minimum fitness value of ISSA means the highest convergence accuracy. The first inflection point indicates that the ISSA curve converges fastest.

Fig.11 shows the inversion error of single-step load. The BPNN models optimized by the five optimization algorithms can accurately reflect the joint mandrel temperature. Among them, the inversion error of ISAA-BPNN and MSWOA-BPNN is the smallest, and the maximum error does not exceed 0.2 °C. The PSO-BPNN error is the largest, but the maximum error does not exceed 0.7 °C. When the load does not fluctuate greatly, the accuracy of each algorithm is high, and the advantage of ISSA is not easy to reflect.

Compared with the single step working condition, as shown in Fig.12, the joint temperature inversion error under multi-step load is generally increased, but the ISSA-BPNN still has excellent performance, and the error is stably distributed within 0.5 °C. The inversion error of other
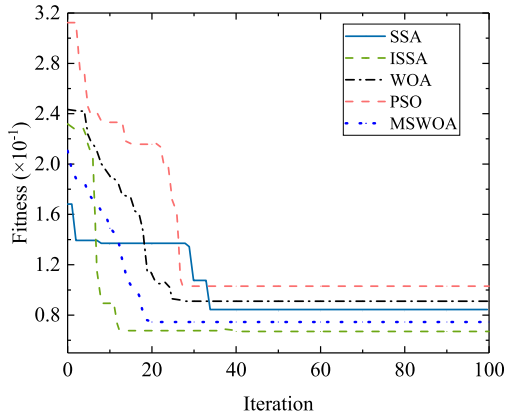
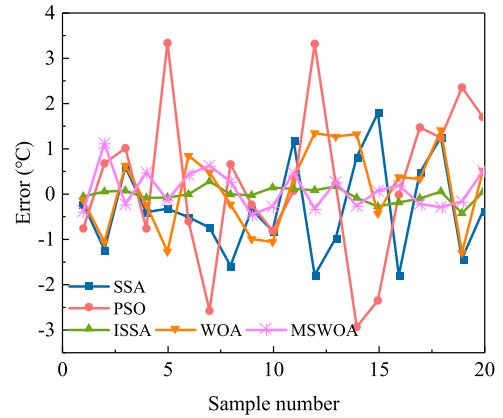**FIGURE 10.** Comparison of fitness curves for five optimization algorithms.
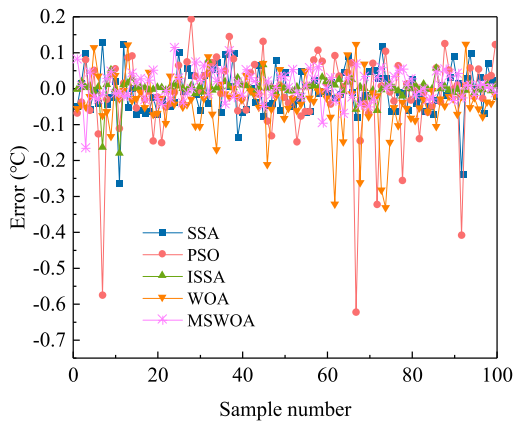

FIGURE 11. Error comparison of temperature inversion results for 110kV cable joints under single step load currents test.

FIGURE 12. Error comparison of temperature inversion results for 110kV cable joints under multi-step load currents test.
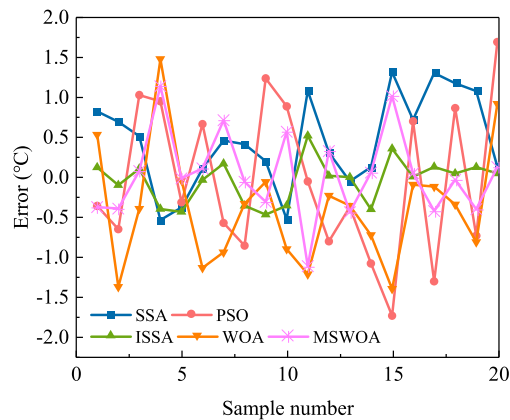

FIGURE 13. Error comparison of temperature inversion results for 110kV cable joints under equivalent actual load current test.

TABLE 6. Comparison of evaluation indexes of multi-step inversion performance of FIVE models.

Model	Evaluating index	Multi-step
SSA-BPNN	δ_{MAE}	0.6955
	δ_{MAPE}	0.015
	δ_{MSE}	0.59
	R^2	0.987
PSO-BPNN	δ_{MAE}	0.782
	δ_{MAPE}	0.017
	δ_{MSE}	0.78
	R^2	0.983
GWO-BPNN	δ_{MAE}	0.698
	δ_{MAPE}	0.015
	δ_{MSE}	0.61
	R^2	0.984
MSWOA-BPNN	δ_{MAE}	0.332
	δ_{MAPE}	0.087
	δ_{MSE}	0.167
	R^2	0.991
ISSA-BPNN	δ_{MAE}	0.210
	δ_{MAPE}	0.0043
	δ_{MSE}	0.075
	R^2	0.998

the R^2 of ISSA-BPNN and MSWOA-BPNN are more than 99%, but the former reaches 99.84%, which is closer to 1, and the error is closer to 0. Combined with Fig.12 and Fig.13, it can be seen that under dynamic load, with the acceleration of load change time, the inversion effect of the neural network model optimized by the original heuristic algorithm becomes worse. However, the performance of ISSA-BPNN is stable, the fluctuation of inversion error is small, and the change of load current size and change rate has little effect on the model inversion effect. It shows that the improved model has strong generalization ability.

C. THE TRANSFERRING ABILITY AND ROBUSTNESS OF THE TEMPERATURE INVERSION METHOD

To further verify the generalization capability of the model, a straight joint for 10 kV 185 mm^2 cable was replaced for a three-day thermal cycling test. The inversion validation was performed based on the data obtained from the tests. As can be seen from Fig.7, the environmental conditions of the test
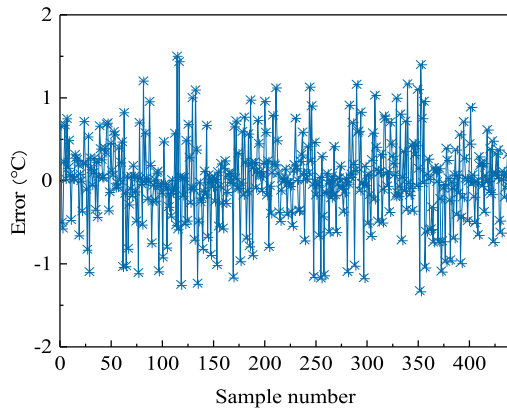
algorithms is increased significantly, compared with Fig.5 especially at sample number 4, 10, 11, 15. These points are the load step change points, this is due to the influence of heat capacity and thermal resistance, thermal time constant lead to load changes, the temperature change of the joint line core reflected in the surface will appear lag phenomenon.

Taking multi-step loading as an example, the inversion effects of five models are evaluated. As shown in Table 6,

FIGURE 14. Error comparison of temperature inversion results for joints of 10kV cable.

were different for each day, and the changes in the surface temperature curve can be seen in the periods of 33-38 and 51-60. The surface temperature fluctuations were very large and unstable, which might be due to the measurement device problems, and the data could not characterize the actual state of the joint and should be discarded. Based on the remaining data, the model was trained and the results were obtained as shown in Fig.14. It can be seen that the error of inversion results remained within 1 °C after replacing the experimental object, and the average absolute error was only 0.35 °C.

VI. CONCLUSION

In this paper, the temperature inversion method based on ISSA-BPNN was used to get cable straight joint core temperature by using surface temperature and cable dynamic load currents. The robustness of this method was validated by temperature-rise tests compared with algorithms. The temperature inversion results in this paper have high accuracy and faster convergence speed. The inversion method based on five optimization algorithms performs well under stable load currents. The inversion performance of the model in this paper is stable and not affected by the speed of the load currents fluctuate. The noise introduced by the actual temperature measurement has little effect on the model inversion accuracy, has strong robustness, and is less affected by the external environment. And it has certain applicability to the joints of different specifications and types.

REFERENCES

[1] Y. Liang, "Technological development in evaluating the temperature and ampacity of power cables," *High Voltage Eng.*, vol. 42, no. 4, pp. 1142–1150, 2016.

[2] C. Bates, K. Malmedal, and D. Cain, "Cable ampacity calculations: A comparison of methods," *IEEE Trans. Ind. Appl.*, vol. 52, no. 1, pp. 112–118, Jan./Feb. 2016.

[3] R. S. Singh, S. Cobben, and V. Ćuk, "PMU-based cable temperature monitoring and thermal assessment for dynamic line rating," *IEEE Trans. Power Del.*, vol. 36, no. 3, pp. 1859–1868, Jun. 2021.

[4] G. Callender, K. F. Goddard, J. K. Dix, and P. L. Lewin, "A flexible model to calculate buried cable ampacity in complex environments," *IEEE Trans. Power Del.*, vol. 37, no. 3, pp. 2007–2015, Jun. 2022.

[5] R. V. Carvalho, M. J. D. C. Bonfim, D. A. Ussuna, L. F. R. B. Toledo, R. Martins, and V. S. Filho, "Distributed temperature sensing in OPGW with multiple optical fibres," *IET Sci., Meas. Technol.*, vol. 13, no. 8, pp. 1219–1223, Oct. 2019.

[6] Q. Zhan, W. Xiao, R. Luo, and T. Tan, "The temperature monitoring of cable joint conductor based on transient thermal circuit model and inversion algorithm," *Southern Power Syst. Technol.*, vol. 8, no. 2, pp. 83–87, 2014.

[7] G.-Y. Kwon and Y.-J. Shin, "Condition monitoring technique of HTS cable via tangent distance-based template matching coefficient," *IEEE Trans. Appl. Supercond.*, vol. 31, no. 5, pp. 1–5, Aug. 2021.

[8] E. F. Steennis, P. Wagenaars, P. van der Wielen, P. Wouters, Y. Li, T. Broersma, and P. Bleeker, "Guarding MV cables on-line: With travelling wave based temperature monitoring, fault location, PD location and PD related remaining life aspects," *IEEE Trans. Dielectr. Electr. Insul.*, vol. 23, no. 3, pp. 1562–1569, Jun. 2016.

[9] T. Lauber and G. Lees, "Enhanced temperature measurement performance: Fusing DTS and DAS results," *IEEE Sensors J.*, vol. 21, no. 6, pp. 7948–7953, Mar. 2021.

[10] A. Z. E. D. Mohamed, H. G. Zaini, O. E. Gouda, and S. S. M. Ghoneim, "Mitigation of magnetic flux density of underground power cable and its conductor temperature based on FEM," *IEEE Access*, vol. 9, pp. 146592–146602, 2021.

[11] Q. Li, Y. Xin, and S. Wang, "Dependence of AC loss on structural compactness of superconducting power cables with narrow coated conductors," *IEEE Trans. Appl. Supercond.*, vol. 26, no. 7, pp. 1–5, Oct. 2016.

[12] D. I. Doukas, A. I. Chrysochos, T. A. Papadopoulos, D. P. Labridis, L. Harnefors, and G. Velotto, "Coupled electro-thermal transient analysis of superconducting DC transmission systems using FDTD and VEM modeling," *IEEE Trans. Appl. Supercond.*, vol. 27, no. 8, pp. 1–8, Dec. 2017.

[13] V. M. Machado, "FEM/BEM hybrid method for magnetic field evaluation due to underground power cables," *IEEE Trans. Magn.*, vol. 46, no. 8, pp. 2876–2879, Aug. 2010.

[14] X. Xu and G. Liu, "Application of a homogeneous Dirichlet boundary condition in the finite element analysis of power cables," *IEEE Trans. Magn.*, vol. 37, no. 3, pp. 1087–1090, May 2001.

[15] Y. Gao, T. Tan, K. Liu, and J. Ruan, "Research on temperature retrieval and fault diagnosis of cable joints," *High Voltage Eng.*, vol. 42, no. 2, pp. 535–542, 2016.

[16] C. Fu, Q. Hao, Y. Liang, and W. Si, "Study on fast calculation method for temperature rise of complex direct soil-buried cable group core," *High Voltage App.*, vol. 57, no. 5, pp. 130–136, May 2021.

[17] J. Ruan, Q. Zhan, L. Tang, and K. Tang, "Real-time temperature estimation of three-core medium-voltage cable joint based on support vector regression," *Energies*, vol. 11, no. 6, p. 1405, May 2018.

[18] B. He, Y. Huang, T. Ye, and H. Xu, "Temperature prediction of cable joint based on PSO-LSSVM predict model," *Electr. Power Eng. Technol.*, vol. 38, no. 1, pp. 31–35, 2019.

[19] P. Wang, G. Liu, H. Ma, Y. Liu, and T. Xu, "Investigation of the ampacity of a prefabricated straight-through joint of high voltage cable," *Energies*, vol. 10, no. 12, p. 2050, Dec. 2017.

[20] M. Fu, Y. Li, S. Pan, J. Dai, and Y. Wang, "Dynamic calculation method of high-voltage cable conductor temperature based on Elman neural network," *High Voltage App.*, vol. 55, no. 10, pp. 121–127, 2019.

[21] Y. Li, T. Han, H. Zhao, and H. Gao, "An adaptive whale optimization algorithm using Gaussian distribution strategies and its application in heterogeneous UCAVs task allocation," *IEEE Access*, vol. 7, pp. 110138–110158, 2019, doi: 10.1109/ACCESS.2019.2933661.

[22] R. Jamal, B. Men, and N. H. Khan, "A novel nature inspired meta-heuristic optimization approach of GWO optimizer for optimal reactive power dispatch problems," *IEEE Access*, vol. 8, pp. 202596–202610, 2020, doi: 10.1109/ACCESS.2020.3031640.

[23] L. Xu, Z. Zhang, X. Chen, S. Zhao, L. Wang, and T. Wang, "Improved sparrow search algorithm based on BP neural network for aero-optics imaging deviation prediction," *J. Optoelectron. Laser*, vol. 32, no. 6, pp. 653–658, 2021.

[24] D. D. Li, Y. X. Wu, and C. C. Zhu, "The parameter determination method of JA hysteresis model based on the sparrow search and genetic algorithm," *High Volt. Eng.*, vol. 43, pp. 1–7, 2021.

[25] Y. Song, Y. Shi, B. Liu, and J. Kang, "Optimal dispatch of microgrid based on reverse mutation sparrow search algorithm," *Electr. Power Eng. Technol.*, vol. 41, no. 2, pp. 163–170, 2022.

[26] N. A. Khan, M. Sulaiman, A. J. Aljohani, P. Kumam, and H. Alrabaiah, "Analysis of multi-phase flow through porous media for imbibition phenomena by using the LeNN-WOA-NM algorithm," *IEEE Access*, vol. 8, pp. 196425–196458, 2020, doi: 10.1109/ACCESS.2020.3034053.

[27] Y. Zhang, J. Lin, Z. Hu, N. A. Khan, and M. Sulaiman, "Analysis of third-order nonlinear multi-singular Emden–Fowler equation by using the LeNN-WOA-NM algorithm," *IEEE Access*, vol. 9, pp. 72111–72138, 2021, doi: 10.1109/ACCESS.2021.3078750.

[28] L.-Y. Hsu and H.-T. Hu, "QDCT-based blind color image watermarking with aid of GWO and DnCNN for performance improvement," *IEEE Access*, vol. 9, pp. 155138–155152, 2021, doi: 10.1109/ACCESS.2021.3127917.

[29] J. Zhang, J. Zheng, X. Xie, Z. Lin, and H. Li, "Mayfly sparrow search hybrid algorithm for RFID network planning," *IEEE Sensors J.*, vol. 22, no. 16, pp. 16673–16686, Aug. 2022.

[30] W. Tuerxun, X. Chang, G. Hongyu, J. Zhijie, and Z. Huajian, "Fault diagnosis of wind turbines based on a support vector machine optimized by the sparrow search algorithm," *IEEE Access*, vol. 9, pp. 69307–69315, 2021, doi: 10.1109/ACCESS.2021.3075547.

[31] N. A. Khan, F. S. Alshammari, C. A. T. Romero, M. Sulaiman, and S. Mirjalili, "An optimistic solver for the mathematical model of the flow of Johnson Segalman fluid on the surface of an infinitely long vertical cylinder," *Materials*, vol. 14, no. 24, p. 7798, Dec. 2021.

[32] J. Xue and B. Shen, "A novel swarm intelligence optimization approach: Sparrow search algorithm," *Syst. Sci. Control Eng.*, vol. 8, no. 1, pp. 22–34, 2020.

[33] Y. Li, S. Wang, Q. Chen, and X. Wang, "Comparative study of several new swarm intelligence optimization algorithms," *Comput. Eng. Appl.*, vol. 56, no. 22, pp. 1–12, 2020.

[34] Q. Mao and Q. Zhang, "Improved sparrow algorithm combining Cauchy mutation and opposition-based learning," *J. Frontiers Comput. Sci. Technol.*, vol. 15, no. 6, pp. 1155–1164, 2021.

[35] W. Zhang, S. Liu, and C. Ren, "Mixed strategy to improved sparrow search algorithm," *Comput. Eng. Appl.*, vol. 57, no. 24, pp. 74–82, 2021.

[36] B. Gao, W. Shen, H. Guan, L. Zheng, and W. Zhang, "Research on multistrategy improved evolutionary sparrow search algorithm and its application," *IEEE Access*, vol. 10, pp. 62520–62534, 2022.

[37] Q. Zhan, L. Tang, X. Ou, Y. Liu, K. Tang, R. Chen, G. Li, and J. Wang, "110 kV cable joint temperature computation based on radial basis function neural networks," in *Proc. IEEE Int. Conf. High Voltage Eng. Appl. (ICHVE)*, Sep. 2018, pp. 1–4.

[38] X. Fan, Y. Xie, G. Liu, Y. Zhao, W. Zhu, and J. Zhang, "Insulation dielectric properties of retired high-voltage cables at different temperatures," *Electr. Power Eng. Technol.*, vol. 40, no. 4, pp. 60–66 and 74, 2021.

[39] P. Yan, S. Shang, C. Zhang, N. Yin, X. Zhang, G. Yang, Z. Zhang, and Q. Sun, "Research on the processing of coal mine water source data by optimizing BP neural network algorithm with sparrow search algorithm," *IEEE Access*, vol. 9, pp. 108718–108730, 2021.

[40] X. Qiu, R. Wang, W. Zhang, Z. Zhang, and J. Zhang, "Improved whale optimizer algorithm based on hybrid strategy," *Comput. Eng. Appl.*, vol. 58, no. 1, pp. 70–78, 2022.

JIANGJUN RUAN (Member, IEEE) was born in Zhejiang, China, in 1968. He received the B.S. and Ph.D. degrees in electric machine engineering from the Huazhong University of Science and Technology, Wuhan, China, in 1990 and 1995, respectively. He was a Postdoctoral Researcher with the Wuhan University of Hydraulic and Electric Engineering, Wuhan, in 1998. He is currently a Professor with the School of Electrical Engineering and Automation, Wuhan University. His research interests include electromagnetic field numerical simulation and high-voltage and insulation technology.

HESHENG ZHU was born in Hubei, China, in 1996. He received the B.S. degree from the Harbin University of Science and Technology, Harbin, China, in 2018. He is currently pursuing the master's degree with China Three Gorges University. His current research interests include online monitoring and fault diagnosis of power equipment.

QINGHUA ZHAN was born in Guangdong, in 1977. He received the B.S. degree from the South China University of Technology, Guangzhou, China, and the M.S. degree from Wuhan University, Wuhan, China, in 2021, where he is currently pursuing the Ph.D. degree. He is also a Professor-Level Senior Engineer. His research interest includes power cable condition monitoring.

YULI WANG was born in Hubei, China, in 1998. He received the B.S. degree from the Wuchang Institute of Technology, in 2021. He is currently pursuing the master's degree with China Three Gorges University. His research interests include online monitoring and fault diagnosis of power equipment.

● ● ●